

Highly luminescent hetero-ligand MOF nanocrystals with engineered massive Stokes shift for photonic applications.

J. Perego¹, Charl X. Bezuidenhout¹, I. Villa^{1,4}, F. Cova¹, R. Crapanzano¹, I. Frank^{3,5}, F. Pagano^{3,2}, N. Kratochwill^{3,6}, E. Auffray³, S. Bracco¹, A. Vedda¹, C. Dujardin⁷, P. E. Sozzani¹, F. Meinardi¹, A. Comotti^{1} and A. Monguzzi^{1*}*

¹ Dipartimento di Scienza dei Materiali, Università degli Studi Milano-Bicocca, via R. Cozzi 55, 20125 Milano – ITALY

² Dipartimento di Fisica “Giuseppe Occhialini”, Università degli Studi Milano-Bicocca, Piazza della Scienza 3, 20126 Milano – ITALY

³ CERN, Geneva, Switzerland

⁴ FZU Institute of Physics, Academy of Sciences of the Czech Republic, Prague – Czech Republic

⁵ Ludwig Maximilian University of Munich, Geschwister-Scholl-Platz 1, Munich, Germany

⁶ University of Vienna, Vienna, Austria

⁷ Institut Lumière Matière, UMR5306 Université Lyon 1-CNRS, Université de Lyon, 69622 Villeurbanne cedex, France

E-mail: angelo.monguzzi@unimib.it

Abstract

An high efficiency emission with a massive Stokes shift is obtained by fluorescent conjugated acene building blocks arranged in nanocrystals. The two ligands of equal molecular length and connectivity, yet complementary electronic properties, are co-assembled by zirconium oxy-hydroxy clusters, generating highly crystalline hetero-MOF nanoparticles. The fast diffusion of singlet molecular excitons in the framework, coupled with the fine matching of ligands absorption and emission properties, enables to achieve an ultrafast activation of the low energy emission by diffusion-mediated non-radiative energy transfer in the 100 ps time scale, by using a low amount of co-ligands. This allow to obtain MOF nanocrystals with a fluorescence quantum efficiency of ~70% and an actual Stokes shift as large as 750 meV. This large Stokes shift suppresses the reabsorption of fast emission issues in bulk devices, pivotal for a plethora of applications in photonics and photon managing spacing from solar technologies, imaging, and detection of high energy radiation. These features allowed to realize a prototypal fast nanocomposite scintillator that shows an enhanced performance with respect to the homo-ligand nanocrystals, achieving benchmark. values which compete with those of some inorganic and organic commercial systems.

The Stokes shift is an important property of luminescent materials, defined as the energy difference (ΔE) between the absorption band maximum and the emission spectrum maximum frequencies.¹ The value of ΔE is a key parameter in photonic devices and applications because, at a first approximation, it enables to estimate if a specific emitter would be affected by significant reabsorption of the generated light. For example, if the ΔE value is lower or similar to the bandwidth of the absorption and emission spectra, the consequent intrinsic extensive ‘inner-filter’ effect can heavily limit the lighting performance of bulk photonic devices, and, in the worst cases, it can also affect the kinetics of the luminescence generation.²⁻⁴ Conversely, if ΔE is larger than the spectral bandwidths the system can be considered a large Stokes shift emitter, with no inner filter effects (Fig. 1a). These reabsorption-free materials are highly desirable for several applications. For example, in fluorescence imaging large Stokes shift optical probes allow to obtain high contrast images with limited excitation stray light, avoiding the use of expensive filtering component or time-consuming image post-processing.^{5,6} For solar applications, large Stokes shift emitters are undoubtedly the most promising materials to realize luminescent solar concentrators without reabsorption of the condensed radiation.⁷ Similarly, the sensitivity of scintillating detectors for ionizing radiation would greatly benefit from the use of fast emitters with no reabsorption⁸ showing good light output intensity without effects on the scintillation pulse timing, as required by the most advanced medical imaging techniques such as time-of-flight positron emission tomography (TOF-PET)⁹ and high-rate high-energy physics (HEP) experiments.

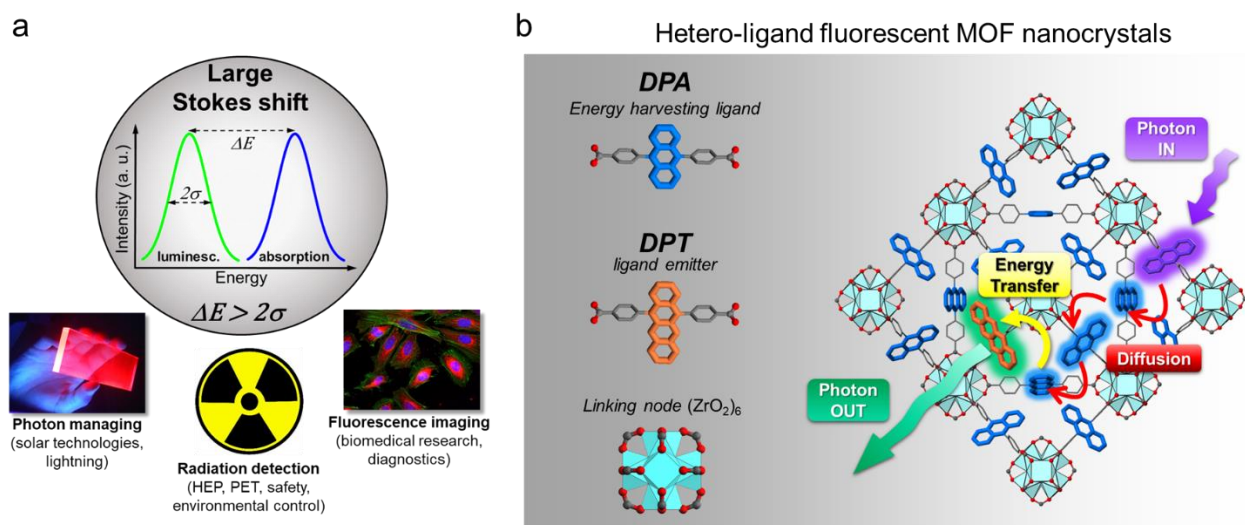


Figure 1 | Large Stokes shift emitters concept, applications and realization with engineered hetero-ligand MOF nanocrystals based on fluorescent ligands. **a**, Definition of large Stokes shift emitter. The energy difference between absorption and luminescence maxima ΔE is larger than luminescence half-height bandwidth 2σ , thus avoiding reabsorption. **b**, (left) Molecular structure of the MOF nanocrystals building blocks, namely the 9,10-diphenyl-antracenedicarboxylate fluorescent ligand (DPA), the 5,12-diphenyl-tetracenedicarboxylate fluorescent co-ligand (DPT) and the linking node zirconium oxo-hydroxy cluster. (right) Sketch of the energy flux after generation of a DPA singlet exciton, in this case upon absorption of a UV photon of energy $h\nu_{in}$. The singlet exciton diffuses within the crystalline framework until it reaches the co-ligand DPT. The latter is excited by non-radiative energy transfer and then recombines radiatively by emitting a green photon of energy $h\nu_{out}$ with a Stokes shift $\Delta E = h\nu_{in} - h\nu_{out}$.

The extensive recent literature in the field of semiconductor nanocrystals testifies this very actual interest on large Stokes shift emitters. In these materials, for example, the ΔE can be tuned by doping of semiconductor with electronic impurities,¹¹ resulting in the appearance of intragap states from which red shifted luminescence is produced. A notable ΔE value as large as 1 eV can be achieved,¹²

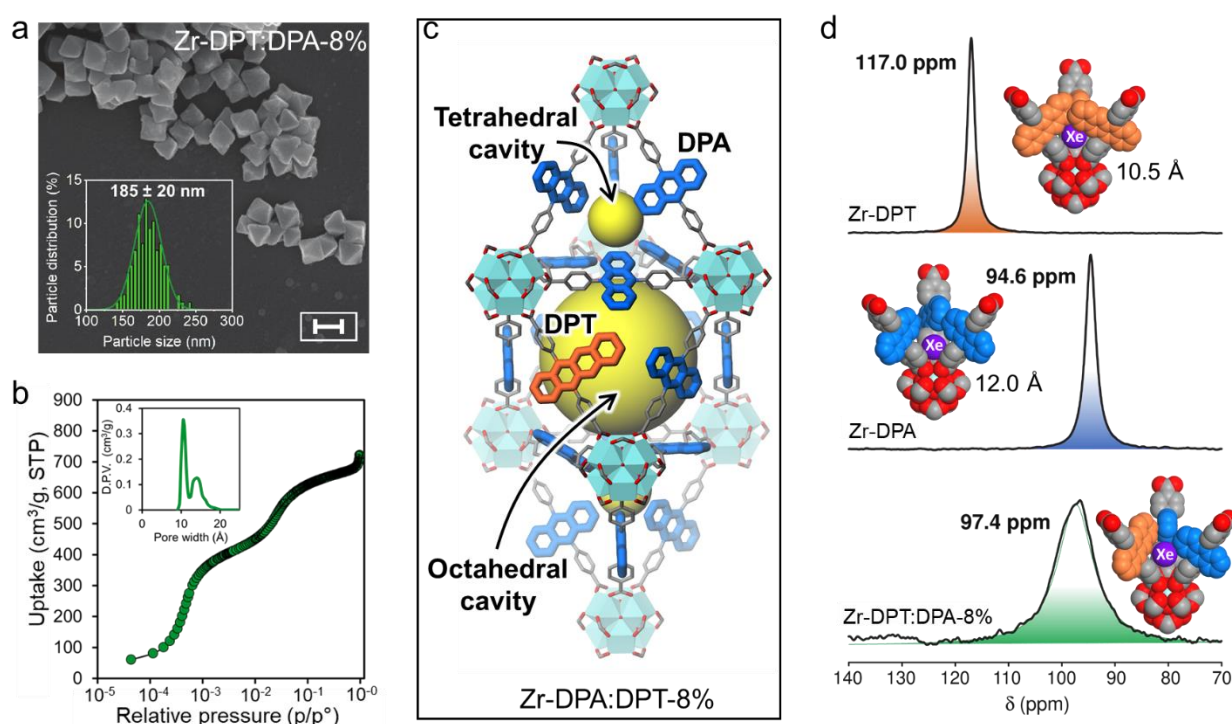
but a current unsolved drawback is the slow luminescence kinetics that strongly limit their use for fast timing applications in nanosecond time scale and below.^{10,13,14} Moreover, in photonic devices where fast timing is foreseen, traditional wavelength shifters exploiting radiative energy transfer cannot be employed, because of the consequent slowing down of emitted light pulse.

In the search for fast emitters with remarkably large Stokes shift, we selected Metal-Organic Frameworks (MOFs), which constitute a solid platform to build materials wherein active struts perform tailored functions. Synthetic procedures based on self-assembly processes enable the controlled framing of struts in the porous crystalline architecture and the regulation of distances among linkers.^{15,16} The impressive versatility of MOFs promoted several applications such as gas storage,^{17,18} catalysis and dynamic materials,¹⁹⁻²³ and triggered the most recent advances in the field of luminescent MOFs.²⁴⁻²⁹ This hot topic gave birth to a new class of optically active nanomaterials with tailorable electronic properties for photonics and optoelectronics, sensing, and biomedicine.^{26,30,31} MOFs are also excellent candidates to be used in light-emitting devices, due to their structural diversity and tunable emission. A key advantage is the possibility to design their framework composition and structure which control both optical and energy-transport properties, such as those required for managing site specific photoreactions,³² or multi-excitonic processes.³³ Therefore, optimized luminescent MOF nanocrystals can represent the next generation of luminescent materials with a potential impact comparable to their inorganic counterpart colloidal semiconductor nanocrystals.

Among conjugated molecules, polycyclic aromatic hydrocarbons of acene family have attracted great interest for various application in photon managing such as photon upconversion and singlet fission because of their peculiar electronic properties.³⁴⁻³⁷ Here we present the fabrication of MOF nanocrystals with fine-tuned composition, wherein tetracene-bearing fluorescent moieties were co-assembled with anthracene-based linkers to engineer the system emission properties and obtain significant energy down conversion of the emitted photons with respect the absorption, thus maximizing the emission Stokes shift. MOFs containing linear tetracene linkers have not yet been realized so far. The strategy of increasing the number of fused aromatic rings in the ligand core, yet maintaining a constant spacing between the chelating groups, proved successful in providing a series of customized *hetero*-ligand Zr-MOFs, which exhibited benchmark-efficiency fluorescence accompanied with negligible reabsorption. MOF nanocrystals were obtained by co-assembling the green-fluorescent chromophore 5,12-*diphenyl-tetracenedicarboxylate* (DPT) and the blue-emitting ligand 9,10-*diphenyl-anthracenedicarboxylate* (DPA) with Zr oxy-hydroxy nodes (Fig.1b). By exploiting the diffusion within the crystalline framework of singlet molecular excitons generated on DPA ligands, the incorporated DPT co-ligands are excited by means of non-radiative energy transfer and subsequently recombine radiatively producing photons with a ΔE as large as 750 meV. The fine matching of frequency emission of anthracene moieties with the absorption of tetracene units enables an efficient energy transfer (ET) of 97% and photoluminescence quantum yield (QY) of ~70% even with a low DPT loading of 8% with respect to DPA (denoted Zr-DPT:DPA-8%). Such a low loading enables to preserve the structural features of the parent *homo*-ligand nanocrystals. The potential technological transfer of the obtained *hetero*-ligand fluorescent nanomaterials is demonstrated by the realization of a prototypal fast polymeric nanocomposite scintillator that shows enhanced performances with respect to the homo-ligand nanocrystals, thus achieving benchmark values competing with those of several organic and inorganic commercial systems.

We designed and prepared the new conjugated tetracene-containing ligand (DPT) to be co-assembled with the anthracene-based linker (DPA) by a solvothermal process (Methods and Supplementary Information): the two molecules DPA (QY=0.96) and DPT (QY=0.80) were chosen

121 because of their complementary of absorption/emission properties that make them an ideal donor
 122 (DPA) and acceptor (DPT) pair for non-radiative energy transfer (Supplementary Information). The
 123 two rod-like ligands with identical end-to-end length and connectivity were co-assembled by
 124 zirconium oxy-hydroxy clusters, generating a series of isostructural *hetero*-ligand MOF nanocrystals
 125 with modulated composition ranging from 0.1% to 8% of DPT/DPA ligand ratio content (Zr-
 126 DPT:DPA-x%, Fig.1b). For comparison, the *homo*-ligand MOFs were synthesized using separately
 127 the single ligands (Zr-DPA and Zr-DPT, respectively). The composition of *hetero*-ligand Zr-MOFs
 128 is in agreement with the feeding ratio, as shown by ^1H NMR of digested samples. Connectivity,
 129 purity, and thermal stability were demonstrated by FT-IR, ^{13}C MAS NMR and TGA analysis
 130 (Supplementary Figs. S1-S40). Scanning electron microscopy (SEM) images of the Zr-DPT:DPA
 131 specimens reveal a homogenous population of nanocrystals with octahedral morphology. Figure 2a
 132 depicts the SEM image of the Zr-DPT:DPA-8% sample, which consists in a nanocrystal ensemble
 133 with average size of 185 ± 20 nm.



134

135 **Figure 2 | *Hetero*-ligand zirconium-based metal-organic framework (MOF) nanocrystals structural properties.** **a,**
 136 Scanning electron microscopy image of MOF nanocrystals realized with a DPT/DPA ligand ratio of 8% (Zr-DPT:DPA-
 137 8%). The inset reports the distribution of MOF size (Scale bar: 200 nm). **b,** N_2 adsorption isotherm collected at 77 K. The
 138 inset showed the pore size distribution with two distinct cavities of 10.8 Å and 14.5 Å. **c,** Crystal structure of Zr-DPT:DPA
 139 highlighting the tetrahedral and octahedral cavities (yellow spheres). **d,** Hyperpolarized laser-assisted ^{129}Xe NMR spectra
 140 of *hetero*-ligand nanocrystals compared with *homo*-ligand MOFs based on DPA and DPT.

141 Upon activation at 130°C under vacuum, the *hetero*-ligand Zr-MOF nanocrystals exhibit a high
 142 crystallinity and a cubic crystal structure ($Fm-3m$) with **fcu** topology, as established by PXRD
 143 Rietveld refinement, which corresponds to that of parent Zr-DPA and Zr-DPT MOFs (Supplementary
 144 Figs. S13-S17). Twelve ligands coordinate to each Zr-based node ($\text{Zr}_6(\mu_3\text{-O})_4(\mu_3\text{-OH})_4(\text{CO}_2)_{12}$
 145 cluster) and yield a framework containing interconnected octahedral and tetrahedral cavities (Fig.2c).
 146 Thus, the ligands are arranged at a sufficiently short center-to-center distance of 11.7 Å that enables
 147 both fast exciton diffusion and non-radiative energy transfer (Supplementary Information).
 148 Consistently with the crystal structure, N_2 adsorption isotherms at 77 K (Fig.2b) showed remarkable
 149 surface areas up to $3000 \text{ m}^2/\text{g}$ and step-wise profiles due to the subsequent filling of the well-

150 differentiated tetrahedral and octahedral cavities with pore size of 10.8 Å and 14.5 Å in the
151 framework. The size, symmetry and homogeneity of the pores were probed by the highly sensitive
152 hyperpolarized laser-assisted ^{129}Xe NMR (Fig. 2d). The *homo*-ligand Zr-DPA and Zr-DPT MOFs
153 show a single sharp signal at $\delta=94.6$ and $\delta=117.0$ ppm, respectively, reflecting the patency of the
154 cavities and the smaller size in Zr-DPT caused by the long flag-like conjugated tetracene moiety
155 protruding into the nanochannels, with a steric encumbrance larger than that of anthracene unit. The
156 *hetero*-ligand Zr-DPT:DPA-8% MOF exhibits a chemical shift at $\delta=96.5$ ppm which corresponds
157 precisely to the expected weighted-average of the two chemical shifts of the *homo*-ligand
158 nanocrystals. Remarkably, no residual signals of the *homo*-ligand MOFs are present, demonstrating
159 the excellent structural homogeneity of the co-assembled nanocrystal ensemble.

160 The photophysical properties of the obtained MOF nanocrystals are investigated by means of
161 photoluminescence spectroscopy. Figure 3a shows the optical absorption and continuous wave
162 photoluminescence spectra of the *hetero*-ligand Zr-DPT:DPA-1% in tetrahydrofuran dispersion (0.1,
163 mg mL^{-1}). We observe a main absorption band in the near-UV spectral matching the profile of the
164 Zr-DPA reference sample, because the absorption of the few DPT substituents is negligible. Upon
165 photoexcitation at 355 nm, the *hetero*-ligand nanocrystals show a broad luminescence in the visible
166 spectrum. The most intense emission peaked at 515 nm and its vibronic replicas at 550 nm and 590
167 nm match the photoluminescence profile of the isolated DPT ligand (Fig.S7) and of the Zr-DPT MOF
168 as a control sample. MOFs. This result suggests that the green luminescence is generated by the
169 radiative recombination of singlet excitons on DPT co-ligands populated by energy transfer from
170 directly excited DPAs ligands, as demonstrated by the excitation photoluminescence spectrum
171 recorded at 540 nm that follows the DPA absorption profile (Fig.3a). The weak residual blue
172 luminescence peaked at 430 nm mirrors an energy transfer yield (ϕ_{ET}) lower than unity. Nevertheless,
173 the presence of this residual emission is crucial to investigate the antenna effect sketched in Fig.1b
174 that occurs in the framework. Figure 3b depicts the normalized photoluminescence spectra of the Zr-
175 DPT:DPA-1% dispersion at different dilution ratios. Notably, the relative intensity of the green and
176 blue emission components is unchanged. This is a crucial result, because if DPAs and DPTs
177 experienced radiative energy transfer as two separated entities, i.e. in a standard bicomponent
178 solution, the ϕ_{ET} value should decrease following the solution dilution level that reduces the
179 concentration of the energy acceptor DPT and therefore the transfer probability.^{1,38} Consequently, the
180 relative intensity of the green *vs.* blue component should be reduced as well. Conversely, the data
181 clearly indicate that ϕ_{ET} is independent from the DPT dilution, thus demonstrating that each
182 nanocrystal works as an individual emitter whose green luminescence is activated by *intra*-crystal
183 energy transfer.

184 This picture is confirmed by time resolved experiments. The top inset of Fig.3b shows the
185 photoluminescence intensity decay with time at 430 nm as a function of the dilution level. The signal
186 decay in the *hetero*-ligand MOF is faster than in the Zr-DPA reference, indicating an efficient energy
187 transfer (*vide infra*),¹ but still no change in the decay kinetic is observed at different dilutions, thus
188 demonstrating that the DPA-DPT interaction is unaffected. Similarly, the bottom inset shows that the
189 green photoluminescence intensity at 540 nm decays with time as a single exponential function with
190 a characteristic lifetime of $\tau \sim 11$ ns (Supporting Table 7) regardless of the dilution level. This is
191 another key result, indeed, the observed lifetime is almost identical to that one of the DPT molecule
192 (11.5 ns, Fig.S41), and is significantly longer with respect to the reference *homo*-ligand DPT-MOFs
193 (7.7 ns, Supporting Table 7). These findings suggest that co-assembled DPT ligands are effectively
194 incorporated and framed as non-interacting single molecules within the nanocrystal architecture and
195 preserve their excellent luminescence properties pivotal for the fabrication of photonic devices.

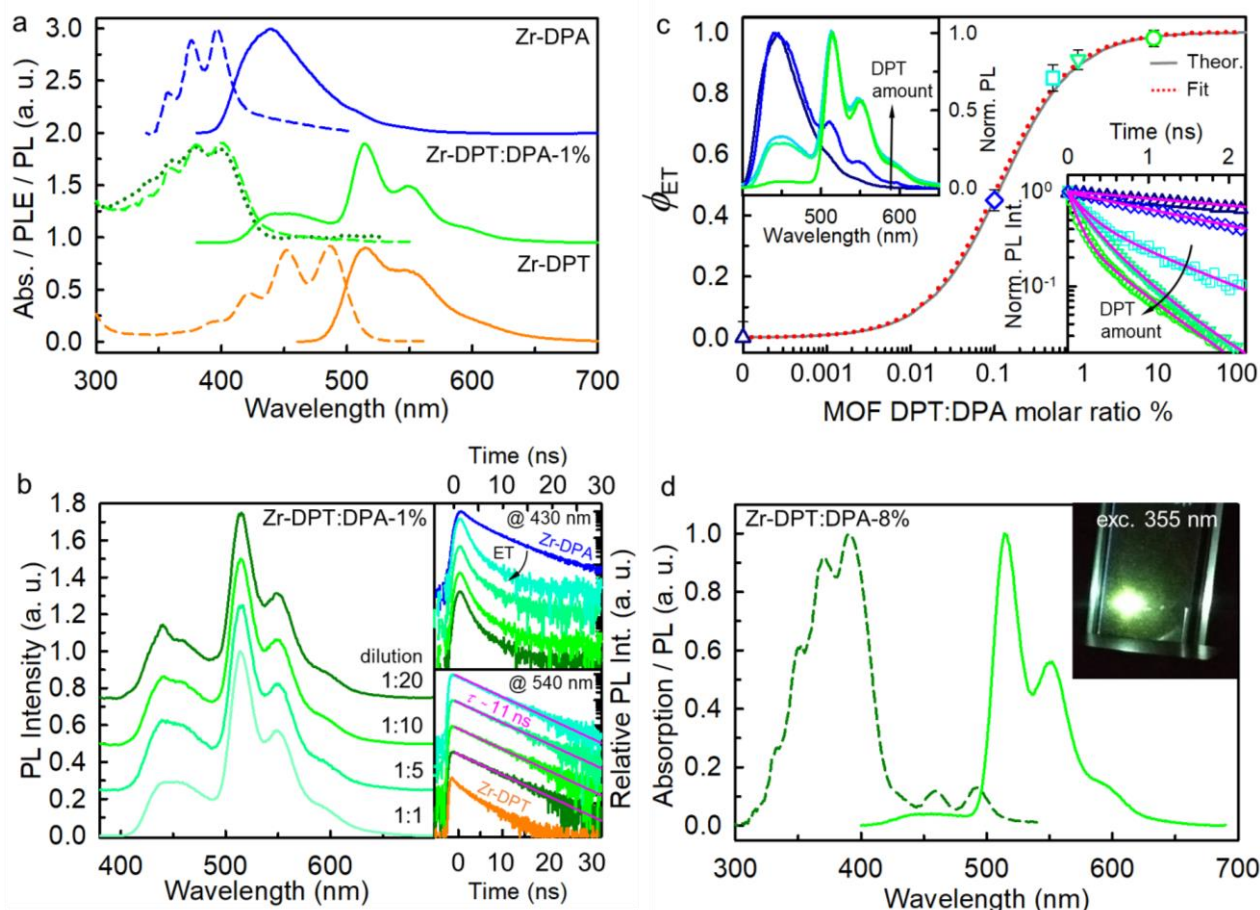


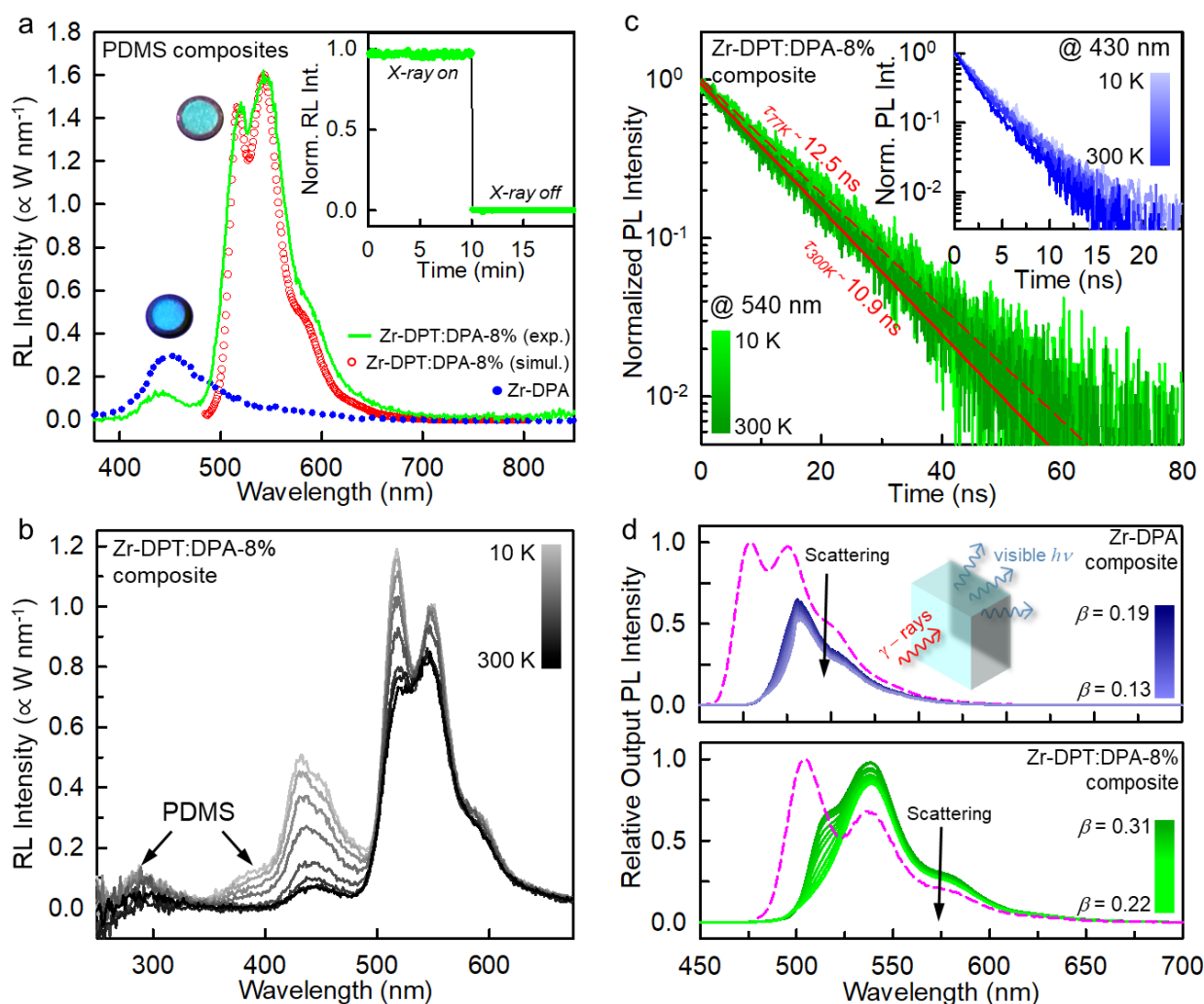
Figure 3 | Photophysical properties of hetero-ligand MOF nanocrystals. **a**, Normalized absorption (dashed line) and photoluminescence (PL, solid line) spectra of the hetero-ligand Zr-DPT:DPA-1% nanocrystals (0.1 mg mL^{-1} in tetrahydrofuran) compared with homo-ligand MOFs based on DPA (Zr-DPA, 0.1 mg mL^{-1}) and DPT (Zr-DPT, 0.1 mg mL^{-1}). The excitation wavelength is 405 nm. The dotted line is the excitation photoluminescence spectrum of the hetero-ligand MOF dispersion recorded at 550 nm **b**, PL spectrum of the Zr-DPT:DPA-1% dispersion at different dilution ratios under 355 laser excitation. The insets show the PL intensity decay with time at 430 nm (top) and 540 nm (bottom) in comparison with that one of Zr-DPA and Zr-DPT reference nanocrystals, respectively. **c**, Energy transfer efficiency ϕ_{ET} between DPA and DPT co-ligands as a function of their relative molar ratio in the MOF framework. The theoretical ϕ_{ET} (solid line) is calculated considering a diffusion-mediated Förster energy transfer with interaction radius of 2.8 nm derived from ligands properties. The fit of experimental data (dotted line) results a characteristic interaction radius of 2.9 nm. The top inset shows the PL spectra of the series of nanocrystals dispersions analyzed (0.1 mg mL^{-1}). The bottom inset show their time-resolved PL spectra recorded at 430 nm. Solid lines are the fit of the data with multi-exponential decay function. **d**, Absorption (dashed line) and PL (solid line) spectrum of Zr-DPT:DPA-1% nanocrystals dispersion (0.1 mg mL^{-1} , optical path 1 cm). The excitation wavelength is 355 nm. The inset is a digital picture of the dispersion in the quartz cuvette under 355 nm excitation.

Once assessed the validity of the synthetic strategy, we investigate quantitatively the energy transfer mechanism. As sketched in Fig.1b, the activation of DPT luminescence occurs by energy transfer during the random diffusion within the framework of an excited DPA singlet exciton, which is created upon light absorption or free-charge recombination in scintillation.³⁹ Before spontaneous recombination, the singlet moves from the original position by an average diffusion length L .⁴⁰⁻⁴² This implies that if a DPT moiety is placed at a distance shorter than L from the position where the DPA exciton is created, the energy transfer can most likely occur before singlet recombination, thus without energy dispersion. Considering the MOF structure and a DPA-DPT Förster interaction radius of $R_{fs} = 2.8 \text{ nm}$ (Fig. S42), the theoretical energy transfer rate k_{ET} and efficiency ϕ_{ET} are calculated as a function of the nanocrystal composition under the assumption of a diffusion-mediated energy

process (Supplementary Material).³⁸ The solid line in Fig.3c depicts the theoretical ϕ_{ET} vs. the DPT ligand fraction in the *hetero*-ligand MOFs, expressed as the nominal DPT:DPA relative molar ratio employed for the synthesis. The plot shows that an excellent $\phi_{ET} \sim 0.9$ (90%) is reached with a DPT content as low as 1%. This suggests that the proposed strategy to achieve large Stokes shift is already effective with low levels of DPT substitution in the DPA based MOF. In this way the risk to affect the MOF structural properties is minimized. The predicted ϕ_{ET} is compared with the one measured in the series of nanocrystals. The top inset of Figure 3c shows the normalized photoluminescence spectra of the MOF samples dispersed in tetrahydrofuran under 355 nm excitation. The blue emission from DPA ligands is almost completely switched off in the Zr-DPT:DPA-8% sample. The experimental ϕ_{ET} value is calculated from the time resolved photoluminescence data shown in the bottom inset (Supplementary Information). The intensity of the blue luminescence at 430 nm decays as multi-exponential function (Supplementary Table 7), whose average lifetime shortens progressively by increasing the DPT amount, according to the corresponding increment of k_{ET} . The circles in the main panel mark the observed ϕ_{ET} , which increases up to 97% in the Zr-DPT:DPA-8% sample. The fit of data with a diffusion-mediated energy transfer kinetics results in an experimental interaction radius $R_{fs}^* = 2.9$ nm for the DPA/DPT pair, in perfect agreement with the proposed model. It is worth noting that the decay of the negligible residual blue emission intensity shows a biexponential behavior (Fig. 3c inset, Supplementary Information) that indicates the presence of two population of emitters. The fast component (67% of the total signal) has a lifetime $\tau_{fast} = 120$ ps $\approx [k_{ET}]^{-1}$ and accounts for the fraction of fully active large Stokes shift nanocrystals ($\phi_{ET}=1$). The slow component is instead ascribed to a small sub-population of nanocrystals in the ensemble, statistically-containing a lower amount of DPT, where the transfer is not complete ($\phi_{ET}<1$). From this analysis it is straightforward to estimate the photoluminescence quantum efficiency of fully active nanocrystals as $QY = QY^{ens}/0.67 = 0.69 \pm 0.06$, where $QY^{ens} = 0.46 \pm 0.05$ is the photoluminescence yield measured for the ensemble in dispersion (Fig. 3d, Methods). Therefore, a huge photoluminescence Stokes shift of 750 meV with highly efficient emission is achieved while preserving the fast time response that outperforms the one obtained in doped semiconductor quantum dots.^{43 44} Notably, both fast energy transfer and high yield Stokes shifted fluorescence are achieved by using low DPT amounts, thanks to the accurate design of *hetero*-crystals made by co-ligands with identical length and connectivity but strictly complementary optical properties owing to the change of their conjugation length. In such a way, the fast singlet excitons diffusion of the *homo*-ligand MOFs is unaffected by the presence of the acceptor moiety in the *hetero*-ligand structure, enabling ultrafast activation of the low energy emitters. The results obtained highlight therefore once more the potential of composition-tuned MOFs to develop efficient loss-free energy harvesting and transport systems that can mimic, for example, also natural photosynthetic mechanisms where fast energy migration is required.

Given their excellent luminescence properties, we tested the *hetero*-ligand MOF nanocrystals as emitters in bulk scintillating devices typically employed as detector of ionizing radiation where large Stokes shift is usually required to maximize the extraction of scintillation light.⁸ Figure 4a shows the radioluminescence spectrum under soft X-ray exposure of a composite scintillator (thickness 0.1 cm, diameter 1 cm) fabricated by loading Zr-DPT:DPA-8% nanocrystals in a polydimethylsiloxane (PDMS) matrix (0.5% weight, Methods, Figs.S43-S46). The radioluminescence spectrum (solid line) is dominated by a structured green emission peaked at 530 nm with a weak residual emission at 430 nm, suggesting that the scintillation light is produced by radiative recombination of DPT singlet excitons. The absence of reabsorption is demonstrated by the possibility to clearly observe the first vibronic replica in the emission spectrum at 515 nm, as in the diluted dispersion case, despite the high concentration of embedded nanocrystals (Fig. 3d). This result is in excellent agreement with the

270 simulated emission spectrum (circles) calculated considering the light propagation in the device
 271 (Methods). Radioluminescence measurements under continuous irradiation up to around one hundred
 272 Gy demonstrate the emission stability and the absence of long-time phosphorescence due to delayed
 273 carrier recombination (inset of Fig.4a). No significant variation of the radioluminescence intensity
 274 can be observed by heating the sample up to 50 °C, demonstrating a good thermal stability (Fig.S47).
 275 After 30 days of exposure to the atmospheric moisture, a mere 10% reduction of the emission intensity
 276 is observed, demonstrating a good resistance to molecular oxygen despite tendency of tetracene to
 277 photobleaching (Fig.S48).



278

279 **Figure 4 | Luminescence properties of large Stokes shift MOF-based nanocomposites under X-ray exposure.** **a,**
 280 Experimental and simulated radioluminescence (RL) spectrum of nanocomposites based on loaded with *hetero*-ligand
 281 Zr-DPT:DPA-8% and *homo*-ligand Zr-DPA nanocrystals fabricated by using polydimethylsiloxane (PDMS) as host
 282 polymer matrix (0.5% wt, 1 mm thickness) under X-ray exposure (digital pictures). RL intensity as a function of time
 283 (inset). **b,** RL spectrum of the Zr-DPT-DPA-8% nanocomposite as a function of the temperature. **c,** Zr-DPT-DPA-8%
 284 nanocomposite photoluminescence (PL) intensity decay recorded at 530 nm and 430 nm (inset) as function of the
 285 temperature under pulsed laser excitation at 405 nm. **d,** Simulated output emission spectrum and efficiency (β) as a
 286 function of the scattering level (from 0 cm^{-1} to 20 cm^{-1}) in a $10 \times 10 \times 5$ mm scintillator. Dashed lines depict the single
 287 molecule spectrum of the DPA (top) and DPT (bottom) chromophores for reference.

288 The nanocomposite shows a radioluminescence intensity five times greater than the reference
 289 composite made with the *homo*-ligand Zr-DPA (dotted line) which demonstrated a scintillation yield
 290 ϕ_{scint} , defined as the number of emitted photons for each MeV of deposited energy for ionizing
 291 radiation, of approximately 1000 ph MeV⁻¹.³⁹ The obtained data indicates therefore that the prototype

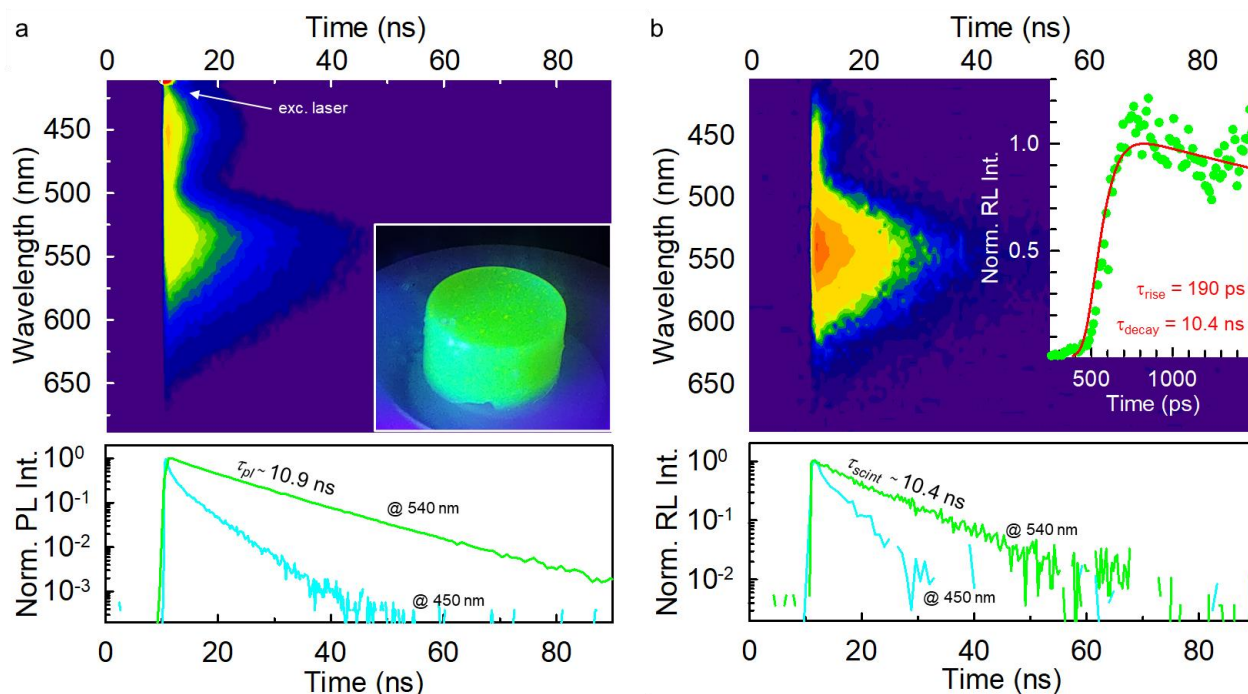
292 ϕ_{scint} is assessed at around 5000 ph MeV⁻¹. This value demonstrates the success of the proposed
293 strategy to enhance the scintillation performance of composite materials based on fluorescent MOF
294 nanocrystals, which show a ϕ_{scint} comparable to that of commercial plastic and inorganic
295 scintillators.⁴⁵

296 We further investigated the composite emission by time resolved photoluminescence and
297 radioluminescence experiments as function of the temperature. At room temperature the composite
298 photoluminescence intensity at 540 nm decays with a characteristic lifetime of 10.9 ns (Fig.4c)
299 matching that of the single molecules (Fig.4b). This finding is crucial to point out an important feature
300 of the *hetero*-ligand emitters. In the case of *homo*-ligand MOFs, the use of high loading levels induces
301 a shortening of the photoluminescence lifetime and efficiency reduction, because of a partial
302 aggregation of poorly dispersed crystals that can limit also the surface passivation effect of the host
303 matrix.³⁹ Conversely, in *hetero*-ligand MOFs this effect appears absent, suggesting that DPT ligands
304 are successfully incorporated as separated and protected units, whose emission ability is insensitive
305 to the nanocrystal environment and aggregation-induced losses.^{39,46} The absence of significant
306 reabsorption is further highlighted by low temperature experiments. By cooling the composite down
307 to 10 K, we still observe the first vibronic replica together with a simultaneous increment of the global
308 green emission intensity (+19%, Fig.4b). This increment is completely ascribed to the suppression of
309 the intramolecular vibrational quenching mechanism at low temperature, as indicated by the emission
310 lifetime that increases up to 12.5 ns at 10 K (+15%, Fig.4c), thus demonstrating the absence of
311 reabsorption-related losses. A more peculiar dynamic is observed for the radioluminescence blue
312 component peaked at 430 nm. At 10 K, we observe a refinement of the vibronic structure in the
313 residual DPA emission, as well as the expected slight lifetime increment (Fig.4b, inset).⁴⁷ However,
314 we observe the simultaneous growth of an overlapped component at 410 nm, which is the main
315 responsible of the blue emission intensity increment, and a UV emission peaked at 280 nm (Fig.S50).
316 Both these components are competitive channels ascribed to the host PDMS. We notice that these
317 electronic transitions are completely dark at 300 K, thus we speculate that they can represent one of
318 the main dissipative pathways that limit ϕ_{scint} due to a non complete energy transfer from the host
319 matrix to the embedded nanocrystals.

320 The scintillation of large Stoke shift nanocomposites is investigated in a bulky cylindrical
321 specimen (diameter 1 cm, height 0.5 cm) loaded with Zr-DPT:DPA-8% (0.5% weight) irradiated with
322 a pulsed X-ray beam (Methods). The expected emission output is reported in Fig.4d, obtained by
323 simulating the propagation of photons in the composites including the scattering and reabsorption /re-
324 emission of travelling photons. The model reproduces a scintillation measurement where a
325 photodetector is coupled by an index-matching on the largest face of the scintillator. The scattering
326 is simulated as an artificial constant absorption background that is superimposed on the material
327 absorption spectrum (Methods). The parameter β is the geometrical detection efficiency, i.e. the
328 fraction of scintillation photons that reaches the photodetector with respect the total number. The
329 obtained results show that the efficiency of the scintillation light outcoupling at low scattering levels
330 ($\beta = 0.31$) is significantly improved with respect to the composite based on the *homo*-ligand MOF
331 Zr-DPA ($\beta = 0.19$). Notably, by exploiting the large Stokes shift nanoscintillators even in very
332 extreme condition with a scattering as large as 20 cm⁻¹, i.e. in the case of fabrication issues that result
333 in an almost completely non-transparent item, the β value assesses to 0.22, thus highlighting the
334 improvement achieved with the proposed material engineering strategy.

335 Fig.5a reports the 2D photoluminescence map of the specimen. Both the spectrum and the
336 photoluminescence intensity decay under pulsed excitation at 405 nm exhibit the same features of the
337 nanocrystal dispersion, i.e. a main emission peak at 540 with lifetime $\tau_{pl} = 10.9$ ns and a residual

338 faster and weaker blue emission showing a multi-exponential decay behavior that reaches the ns time
 339 scale. The 2D scintillation map is showed in Fig.5b. The emission spectrum is analogous to the
 340 photoluminescence, with an intense scintillation band peaked at 540 nm and a weak blue emission at
 341 430 m and same recombination kinetics. More precisely, the green scintillation characteristic lifetime
 342 $\tau_{scint} = 10.4$ ns matches well the τ_{pl} value, thus demonstrating that the MOFs preserve their excellent
 343 emission properties also if used as nanoscintillators. Taking a closer look to the ultrafast time scale,
 344 we observe that the green scintillation flash is well reproduced by a pulse function with an average
 345 decay time $\tau_{decay} = 10.45 = \tau_{scint}$ ns convoluted with the instrumental response function (Methods,
 346 inset of Fig. 5b). The scintillation pulse shows a rise time τ_{rise} of 190 ps, defined as the time variation
 347 between 10% and 90% of the maximum pulse intensity. Considering the speed of the energy transfer
 348 observed, an accurate estimate of the real rise time is therefore partially hindered by the instrumental
 349 response. However, no slow rise time is observed, thus demonstrating that the green scintillation is
 350 activated by the fast non-radiative energy transfer, with no contribution from the residual slow blue
 351 emitters.



352

353 **Figure 5 | Scintillation properties of large Stokes shift MOF-based nanocomposites.** **a**, 2D map of the time resolved
 354 photoluminescence (PL) of the composite under 405 pulse laser excitation. The inset is a digital picture of the composite
 355 under UV lamp exposure. The bottom panel shows the decays in time of the PL intensity recorded at 540 nm and 430 nm.
 356 **b**, 2D map of the composite scintillation emission under pulsed X-rays exposure. The bottom panel highlight the decay
 357 in time of the scintillation pulse intensity recorded at 540 nm and 430 nm. The top panel inset shows the scintillation
 358 pulse recorded in the ultrafast time scale with the instrumental response function (IRF) and the fit of the data with a pulse
 359 function convoluted with the IRF with a given average decay time τ_{decay} of 10.4 ns.

360 These findings demonstrate the success of the designed strategy of mixed acenes in MOFs and,
 361 despite the scintillation rise time cannot be accurately quantified, they suggest that even faster
 362 activation kinetics can be achieved. For example, by employing complementary ligands with better
 363 energetic resonance or by developing high-diffusivity nanocrystals by the fine tuning of the
 364 intermolecular orientation in the MOF framework, it would be possible to further enhance the energy
 365 transfer rate, thus achieving the activation of the Stokes shifted luminescence in times below the 100
 366 ps threshold. These emitters will be therefore the ideal building blocks to realize high-optical quality
 367 bulk composite systems exploiting optimized loading strategies, which will enable to increase the

368 amount of embedded nanoscintillators avoiding aggregation and therefore limiting the scattering of
369 the scintillation light also in large area devices.

370 In conclusion, we successfully engineered the composition of co-assembled *hetero*-ligand
371 MOF nanocrystals obtaining efficient and fast emitters with a large Stokes shift. Thanks to the fast
372 diffusion-mediated non-radiative energy transfer mechanism occurring in the highly ordered
373 crystalline framework between the different species of fluorescent ligands, we achieved a massive
374 Stokes shift of 750 meV. This makes these new nanoemitters ideal candidates for reabsorption-free
375 photonic applications that require fast timing response, thus surpassing the current limitation of large
376 Stokes shift semiconductor nanostructures. The excellent emission quantum yield observed is a direct
377 consequence of the success of the synthetic strategy employed to couple complimentary, fluorescent
378 acene-based building blocks in a MOF architecture. Indeed, the results obtained indicate that the
379 controlled incorporation of the energy acceptor ligands not only does not perturb the structural
380 properties and stability of the MOFs, but also protect the anthracene-emitters from surface-related
381 luminescence quenching observed in *homo*-ligand MOF. Moreover, this strategy allows to protect the
382 emitting ligands from the external environment also in a composite preferred form that exploits a
383 transparent polymer host matrix, overcoming the energy losses related to phase segregation and
384 aggregation. The potential impact of these new nanoemitters is highlighted by the investigation of
385 their scintillation properties. The composite plastic scintillator based on *hetero*-ligand MOFs shows
386 a better scintillation performance with respect to the previously investigated *homo*-ligand
387 nanocrystals, which already demonstrated interesting features for the development of a new family
388 of fast scintillators. Considering that the proposed strategy can be in principle applied to different
389 ligand pairs with resonant electronic energies to tune both the emission Stokes shift and the spectral
390 working ranges (according to specific application requests), the obtained results strongly support the
391 future development of ligand-engineered MOF nanocrystals for photonic and photo-chemical
392 applications that require energy harvesting, site specific collecting as well as photon frequency
393 manipulation.

394

395 **Methods**

396 Synthesis of Zr-DPT. MOF nanocrystals were synthesized under solvothermal conditions modulated
397 by acetic acid. The conditions were optimized to generate a highly crystalline sample. Briefly,
398 ZrCl_4 , 5,12-bis(4-carboxyphenyl) tetracene (DPT) and acetic acid were dispersed in DMF (see SI for
399 further details). The resulting mixture was heated at 120°C for 22 hours and the orange powder was
400 filtered and washed with fresh solvent before activation at 130°C under high vacuum before
401 characterization. The synthesis of DPT ligand is reported in Supporting Information.

402
403 Synthesis of Zr-DPT:DPA-x%. Nanocrystalline samples of Zr-DPT:DPA-x% were synthesized under
404 solvothermal conditions modulated with acetic acid. ZrCl_4 and a proper amount of 5,12-bis(4-
405 carboxyphenyl)tetracene (DPT) and 9,10-bis(4-carboxyphenyl) anthracene (see SI for further details)
406 were dispersed in a mixture of DMF and acetic acid. The mixture was heated at 120°C for 22 hours
407 and the yellowish powder was filtered and washed with fresh solvent before activation at 130°C under
408 high vacuum.

409
410 Synthesis of Zr-MOF:PDMS composites. PDMS nanocomposites were prepared by dispersing MOF
411 nanocrystals in a prepolymer mixture that was poured in a proper mould and cured at 60°C to obtain
412 self-standing nanocomposites. The nanocomposites were obtained by the reaction of vinyl-terminated
413 polydimethylsiloxane with polydimethylsiloxane-co-methylhydrosiloxane by thermal curing. The
414 cross-linking reaction starting from the polymer terminals preserved the flexibility of the polymer
415 chains and produced very low glass transition.⁴⁸

416
417 Structure analysis and microscopy. The structure and composition of Zr-MOF nanocrystals and
418 nanocomposites were determined by means of powder X-ray diffraction (PXRD) structure
419 refinement, nuclear magnetic resonance (NMR) spectroscopy, Fourier - transform infrared (FT-IR)
420 spectroscopy, thermogravimetric analysis (TGA), adsorption properties, helium pycnometry,
421 scanning electron microscopy (SEM) and transmission electron microscopy (TEM). Details on the
422 instrumental setup and the measurement protocols are reported in the supplementary material file.
423 The crystal structures were refined by the Rietveld method combined with molecular mechanics and
424 plane-wave DFT calculations (see Supplementary Material).

425
426 Photoluminescence studies. Absorption spectra has been recorded with a Cary Lambda 900
427 spectrophotometer at normal incidence using quartz Suprasil cuvettes with 0.1 cm of optical path and
428 an integrating sphere to eliminate scattering effects. Steady state photoluminescence (PL) spectra
429 were acquired with a Variant Eclipse fluorimeter (bandwidth 1 nm) using quartz Suprasil cuvettes
430 with 1 cm of optical path. Time-resolved photoluminescence experiments in the nanosecond time
431 scale have been made by using as excitation source a pulsed laser LED at 340 nm (3.65 eV, EP-LED
432 340 Edinburgh Instruments, pulse width 80 ps). Quartz Suprasil cuvettes with 0.1 cm of optical path
433 has been used to study nanocrystals dispersions. The nanocomposites were excited with a pulsed laser
434 at 405 nm (3.06 eV, EPL-405 Edinburgh Instruments, pulse width 90 ps) to avoid direct excitation of
435 the host polymer matrix. Experiments in the picoseconds time scale have been made by using a
436 doubled Ti:Sapph pulsed laser at 380 nm (3.65 eV, Coherent Mira 900, pulse width 150 fs) coupled
437 to a streak camera Hamamatsu Synchroscan M1955. The PL quantum yields of DPT and MOF 8%
438 dispersion have been measured by relative methods as described in the Supplementary Material file.
439 Measurements on composites as a function of the temperature were performed on films 0.1 cm
440 thickness and diameter 1 cm, mounting the sample in closed circle He cryostat with direct optical
441 access.

442
443 Radioluminescence studies. Steady state RL measurements were carried out at room temperature
444 using a homemade apparatus featuring, as a detection system, a liquid nitrogen-cooled, back-

illuminated, and UV-enhanced charge coupled device (CCD) Jobin-Yvon Symphony II, combined with a monochromator Jobin-Yvon Triax 180 equipped with a 100 lines/mm grating. All spectra are corrected for the spectral response of the detection system. RL excitation was obtained by unfiltered X-ray irradiation through a Be window, using a Philips 2274 X-ray tube with tungsten target operated at 20 kV. At this operating voltage, a continuous X-ray spectrum is produced by a Bremsstrahlung mechanism superimposed to the L and M transition lines of tungsten, due to the impact of electrons generated through thermionic effect and accelerated onto a tungsten target. The dose rate was 0.2 Gy/s, evaluated by comparison with a calibrated ^{90}Sr - ^{90}Y beta radioactive source and using optically stimulated luminescence emission from quartz crystalline powder (100 – 200 μm grains). In order to record the PL measurements, the same acquisition system of RL measurements has been coupled to a 405 nm pulsed diode laser (EPL-405 Edinburgh Instruments) through a quartz optical fibre bundle allowing the illumination of the sample in the X-ray chamber.

Scintillation studies. Pulsed X-rays with energies up to 25keV were generated with a repetition rate of 1MHz by a picosecond diode laser at 405nm (Delta diode from Horiba) focused on a X-ray tube (model N5084 from hamamatsu). In the case of optical excitation, the same laser (405nm) was used. The resulting photons were collected by Kymera spectrograph (ANDOR) and detected by an hybrid PMT 140-C from Becker & Hickl GmbH. For decay-time measurements, the photons were histogramed using a PicoHarp300 time-correlated single-photon counting (32ps time/bin) and for the time resolved spectra a MCS6A multiple-channel time analyser was used (800ps time/bin) Sub-nanosecond scintillation emission kinetics of the samples were measured with a Time Correlated Single Photon Counting (TCSPC) setup. As excitation source a pulsed X-Ray beam (X-ray Tube XRT N5084, Hamamatsu), with a continuous energy spectrum between 0 and 40 keV and a mean energy of 9.15 keV, produced with a Pulse Diode Laser (PDL 800-B, PicoQuant) were used. The scintillation light was collected in reflection by a Hybrid Photomultiplier Tube (HPM 100-07, Becker & Hickel), operating in TCSPC mode, and processed by an Amplifier and Timing Discriminator (model 9237, ORTEC). This processed HPM output signal was used as stop signal for a Time to Digital Converter (TDC xTDC4, chronologic), while the start signal was given by the external trigger of the PDL. An optical band-pass filter (450 nm with a FWHM of 40 nm) was used, chosen accordingly to the emission spectrum of the samples, to cut observed air excitation by X-Ray. The scintillation pulse was fitted with a convolution between the Impulse Response Function (IRF) of the whole system with a full width at half maximum (FWHM) of 180 ps and the intrinsic scintillation rate.⁹ Sub-nanosecond scintillation emission kinetics of the samples were measured with a Time Correlated Single Photon Counting (TCSPC) setup. As excitation source a pulsed X-Ray beam (X-ray Tube XRT N5084, Hamamatsu), with a continuous energy spectrum between 0 and 40 keV and a mean energy of 9.15 keV, produced with a Pulse Diode Laser (PDL 800-B, PicoQuant) were used. The scintillation light was collected in reflection by a Hybrid Photomultiplier Tube (HPM 100-07, Becker & Hickel), operating in TCSPC mode, and processed by an Amplifier and Timing Discriminator (model 9237, ORTEC). This processed HPM output signal was used as stop signal for a Time to Digital Converter (TDC xTDC4, chronologic), while the start signal was given by the external trigger of the PDL. An optical band-pass filter (450 nm with a FWHM of 40 nm) was used, chosen accordingly to the emission spectrum of the samples, to cut observed air excitation by X-Ray. The scintillation pulse was fitted with a convolution between the Impulse Response Function (IRF) of the whole system with a full width at half maximum (FWHM) of 180 ps and the intrinsic scintillation rate.⁹

Light propagation modelling. Simulations of the scintillating nanocomposite performances were carried out using a Monte Carlo ray-tracing method previously presented.³⁹ The photon propagation follows geometrical optics laws where the interference is neglected. Each photon can be absorbed and re-emitted by a chromophore, isotropically scattered, and reflected or transmitted at the

interfaces, where the Fresnel coefficients have been used to compute the reflection probability. The simulated scintillator contains the same number of nanocrystals employed to fabricate the described sample. The absorption, scattering, transmission, or reflection events are chosen according to random Monte Carlo drawing. The simulations were performed using the experimental absorption/luminescence spectrum and emission efficiency of nanocrystals ($\Phi_{\text{PL}} = 67\%$ for Zr-DPT:DPA-8% and $\Phi_{\text{PL}} = 27\%$ for Zr-DPA). The scattering is supposed to induce light attenuation corresponding to an absorption coefficient ranging from 0 to 20 cm^{-1} .

Acknowledgements

Financial support from the Italian Ministry of University and Research (MIUR) through grant “Dipartimenti di Eccellenza- 2017 “Materials for Energy” is gratefully acknowledged. The authors acknowledge support from PRIN-20173L7W8K. The work performed at CERN was made in frame of Crystal Clear Collaboration

Author contributions

J.P. and A.C. designed and synthesized the MOF nanocrystals and fabricated the composites. J.P., S.B., P.E.S., C.X.B. and A.C. analysed the nanocrystals and composite structural properties. I.V., R.C., F.C and A.V. performed the radioluminescence studies. C.D., I.F, N.K., F.P and EA performed the scintillation experiments. F.M. and A.M. performed and supervised the photoluminescence studies. F.M. and A.M. developed the numerical modelling of the nanocomposite optical properties. A. C. and A.M. conceived and designed the project.

Competing financial interests

The authors declare no competing financial interests.

Additional information

Supplementary information is available in the online version of the paper. Correspondence and requests for materials should be addressed to A. M..

522 References

- 523 1 Lakowicz, J. R. *Principles of fluorescence spectroscopy*. (Springer Science+Business Media, 2010).
- 524 2 Hehlen, M. P. Reabsorption artifacts in measured excited-state lifetimes of solids. *J. Opt. Soc. Am. B*
525 **14**, 1312-1318 (1997).
- 526 3 Yamada, T., Yamada, Y., Nakaike, Y., Wakamiya, A. & Kanemitsu, Y. Photon Emission and
527 Reabsorption Processes in CH₃NH₃PbBr₃ Single Crystals Revealed by Time-Resolved Two-Photon-
528 Excitation Photoluminescence Microscopy. *Physical Review Applied* **7**, 014001 (2017).
- 529 4 Staub, F., Anusca, I., Lupascu, D. C., Rau, U. & Kirchartz, T. Effect of reabsorption and photon
530 recycling on photoluminescence spectra and transients in lead-halide perovskite crystals. *Journal of*
531 *Physics: Materials* **3**, 025003 (2020).
- 532 5 Zhang, J. *et al.* Highly Stable Near-Infrared Fluorescent Organic Nanoparticles with a Large Stokes
533 Shift for Noninvasive Long-Term Cellular Imaging. *ACS Applied Materials & Interfaces* **7**, 26266-
534 26274 (2015).
- 535 6 Ren, T.-B. *et al.* A General Method To Increase Stokes Shift by Introducing Alternating Vibronic
536 Structures. *Journal of the American Chemical Society* **140**, 7716-7722 (2018).
- 537 7 Mattiello, S. *et al.* Chemically Sustainable Large Stokes Shift Derivatives for High-Performance
538 Large-Area Transparent Luminescent Solar Concentrators. *Joule* **4**, 1988-2003 (2020).
- 539 8 Wang, X. *et al.* Organic phosphors with bright triplet excitons for efficient X-ray-excited
540 luminescence. *Nature Photonics* **15**, 187-192 (2021).
- 541 9 Gundacker, S., Auffray, E., Pauwels, K. & Lecoq, P. Measurement of intrinsic rise times for various
542 L (Y) SO and LuAG scintillators with a general study of prompt photons to achieve 10 ps in TOF-
543 PET. *Physics in Medicine & Biology* **61**, 2802 (2016).
- 544 10 Lecoq, P., Korzhik, M. & Vasiliev, A. Can Transient Phenomena Help Improving Time Resolution in
545 Scintillators? *IEEE Transactions on Nuclear Science* **61**, 229-234 (2014).
- 546 11 Viswanatha, R., Brovelli, S., Pandey, A., Crooker, S. A. & Klimov, V. I. Copper-Doped Inverted
547 Core/Shell Nanocrystals with “Permanent” Optically Active Holes. *Nano Letters* **11**, 4753-4758
548 (2011).
- 549 12 Khan, A. H. *et al.* Tunable and Efficient Red to Near-Infrared Photoluminescence by Synergistic
550 Exploitation of Core and Surface Silver Doping of CdSe Nanoplatelets. *Chemistry of Materials* **31**,
551 1450-1459 (2019).
- 552 13 Pinchetti, V. *et al.* Excitonic pathway to photoinduced magnetism in colloidal nanocrystals with
553 nonmagnetic dopants. *Nature Nanotechnology* **13**, 145-151, doi:10.1038/s41565-017-0024-8 (2018).
- 554 14 Mondal, P., Chakraborty, S., Grandhi, G. K. & Viswanatha, R. Copper Doping in II–VI Semiconductor
555 Nanocrystals: Single-Particle Fluorescence Study. *The Journal of Physical Chemistry Letters* **11**,
556 5367-5372 (2020).
- 557 15 Yaghi, O. M. *et al.* Reticular synthesis and the design of new materials. *Nature* **423**, 705-714 (2003).
- 558 16 Zhou, H.-C. J. & Kitagawa, S. Metal–Organic Frameworks (MOFs). *Chemical Society Reviews* **43**,
559 5415-5418 (2014).
- 560 17 Chen, K.-J. *et al.* Synergistic sorbent separation for one-step ethylene purification from a four-
561 component mixture. *Science* **366**, 241-246 (2019).
- 562 18 Siegelman, R. L., Kim, E. J. & Long, J. R. Porous materials for carbon dioxide separations. *Nature*
563 *Materials* **20**, 1060-1072 (2021).
- 564 19 Rosi, N. L. *et al.* Hydrogen Storage in Microporous Metal–Organic Frameworks. *Science* **300**, 1127
565 (2003).
- 566 20 Dolgoplova, E. A., Rice, A. M., Martin, C. R. & Shustova, N. B. Photochemistry and photophysics
567 of MOFs: steps towards MOF-based sensing enhancements. *Chemical Society Reviews* **47**, 4710-4728
568 (2018).
- 569 21 Bavykina, A. *et al.* Metal–organic frameworks in heterogeneous catalysis: recent progress, new trends,
570 and future perspectives. *Chemical Reviews* **120**, 8468-8535 (2020).
- 571 22 Perego, J. *et al.* Fast motion of molecular rotors in metal–organic framework struts at very low
572 temperatures. *Nature Chemistry* **12**, 845-851 (2020).
- 573 23 Danowski, W. *et al.* Visible-light-driven rotation of molecular motors in a dual-function metal–organic
574 framework enabled by energy transfer. *Journal of the American Chemical Society* **142**, 9048-9056
575 (2020).
- 576 24 Mezenov, Y. A., Krasilin, A. A., Dzyuba, V. P., Nominé, A. & Milichko, V. A. Metal–organic
577 frameworks in modern physics: Highlights and perspectives. *Advanced Science* **6**, 1900506 (2019).

- 578 25 Yin, H.-Q. & Yin, X.-B. Metal–Organic Frameworks with Multiple Luminescence Emissions: Designs
579 and Applications. *Accounts of Chemical Research* **53**, 485-495 (2020).
- 580 26 Lustig, W. P. *et al.* Metal–organic frameworks: functional luminescent and photonic materials for
581 sensing applications. *Chemical Society Reviews* **46**, 3242-3285 (2017).
- 582 27 Castiglioni, F. *et al.* Modulation of porosity in a solid material enabled by bulk photoisomerization of
583 an overcrowded alkene. *Nature Chemistry* **12**, 595-602 (2020).
- 584 28 Jia, J. *et al.* Access to Highly Efficient Energy Transfer in Metal–Organic Frameworks via Mixed
585 Linkers Approach. *Journal of the American Chemical Society* **142**, 8580-8584 (2020).
- 586 29 An, Z. *et al.* Influence of Isomerism on Radioluminescence of Purely Organic Phosphorescence
587 Scintillators. *Angewandte Chemie* (2021).
- 588 30 Kreno, L. E. *et al.* Metal–organic framework materials as chemical sensors. *Chemical reviews* **112**,
589 1105-1125 (2012).
- 590 31 Lu, K. *et al.* Low-dose X-ray radiotherapy–radiodynamic therapy via nanoscale metal–organic
591 frameworks enhances checkpoint blockade immunotherapy. *Nature biomedical engineering* **2**, 600-
592 610 (2018).
- 593 32 Laurier, K. G. M. *et al.* Iron(III)-Based Metal–Organic Frameworks As Visible Light Photocatalysts.
594 *Journal of the American Chemical Society* **135**, 14488-14491 (2013).
- 595 33 Park, J., Xu, M., Li, F. & Zhou, H.-C. 3D Long-Range Triplet Migration in a Water-Stable Metal–
596 Organic Framework for Upconversion-Based Ultralow-Power in Vivo Imaging. *Journal of the*
597 *American Chemical Society* **140**, 5493-5499 (2018).
- 598 34 Ravetz, B. D. *et al.* Photoredox catalysis using infrared light via triplet fusion upconversion. *Nature*
599 **565**, 343-346 (2019).
- 600 35 Einzinger, M. *et al.* Sensitization of silicon by singlet exciton fission in tetracene. *Nature* **571**, 90-94
601 (2019).
- 602 36 Ronchi, A. *et al.* High Photon Upconversion Efficiency with Hybrid Triplet Sensitizers by Ultrafast
603 Hole-Routing in Electronic-Doped Nanocrystals. *Advanced Materials* **32**, 2002953, (2020).
- 604 37 Budden, P. J. *et al.* Singlet exciton fission in a modified acene with improved stability and high
605 photoluminescence yield. *Nature Communications* **12**, 1527 (2021).
- 606 38 Stryer, L., Thomas, D. D. & Meares, C. F. Diffusion-Enhanced Fluorescence Energy Transfer. *Annual*
607 *Review of Biophysics and Bioengineering* **11**, 203-222 (1982).
- 608 39 Perego, J. *et al.* Composite fast scintillators based on high-Z fluorescent metal–organic framework
609 nanocrystals. *Nature Photonics* **15**, 393-400 (2021).
- 610 40 Pope, M. & Swenberg, C. E. *Electronic processes in organic crystals and polymers*. Vol. 39 (Oxford
611 University Press on Demand, 1999).
- 612 41 Scholes, G. D. Long-Range Resonance Energy Transfer in Molecular Systems. *Annual Review of*
613 *Physical Chemistry* **54**, 57-87 (2003).
- 614 42 Mikhnenko, O. V., Blom, P. W. & Nguyen, T.-Q. Exciton diffusion in organic semiconductors. *Energy*
615 *& Environmental Science* **8**, 1867-1888 (2015).
- 616 43 Sahu, A. *et al.* Electronic Impurity Doping in CdSe Nanocrystals. *Nano Letters* **12**, 2587-2594 (2012).
- 617 44 Hughes, K. E., Hartstein, K. H. & Gamelin, D. R. Photodoping and Transient Spectroscopies of
618 Copper-Doped CdSe/CdS Nanocrystals. *ACS Nano* **12**, 718-728 (2018).
- 619 45 Turtos, R. M., Gundacker, S., Auffray, E. & Lecoq, P. Towards a metamaterial approach for fast timing
620 in PET: experimental proof-of-concept. *Physics in Medicine & Biology* **64**, 185018 (2019).
- 621 46 Monguzzi, A. *et al.* Highly Fluorescent Metal–Organic-Framework Nanocomposites for Photonic
622 Applications. *Nano Letters* **18**, 528-534 (2018).
- 623 47 Ware, W. R. & Baldwin, B. A. Effect of Temperature on Fluorescence Quantum Yields in Solution.
624 *The Journal of Chemical Physics* **43**, 1194-1197 (1965).
- 625 48 Bosq, N., Guigo, N., Persello, J. & Sbirrazzuoli, N. Melt and glass crystallization of PDMS and PDMS
626 silica nanocomposites. *Physical Chemistry Chemical Physics* **16**, 7830-7840 (2014).